Progress In Electromagnetics Research B, Vol. 98, 59–75, 2023

Efficient Computation of Sideband Power Losses in Pulse-Shifted Nonuniform Time-Modulated Array with Arbitrary Element Pattern

Sujoy Mandal* **and Sujit K. Mandal**

Abstract—This paper presents the mathematical formulation for the generalized closed-form expressions to calculate sideband power (P_{SR}) of a nonuniform period time modulated array (NTMA) antenna with volumetric geometry by using pulse shifting strategy. For the arbitrary array geometry, the generalized expression of P_{SR} is obtained by considering the universal omnidirectional element pattern in the form $\sin^a\theta\,|\cos\theta|^b$, $a > -1$, $b > -1/2$. Then, corresponding to different array structures such as linear, planar, and volumetric ones, the derived expression is simplified for different element patterns with possible combination of 'a' and 'b'. Through representative numerical results it is demonstrated that the obtained simplified expressions without hypergeometric function are useful to accurately calculate the amount of power losses due to sideband radiations with significantly less time than the conventional numerical integration (NI) method.

1. INTRODUCTION

Over the last two decades, time-modulated array (TMA) has received extensive attention in the application of wireless communication because of its superior, simple, low-cost, and software-based electronically controlled beamforming network [1–3]. Electronically the ON-OFF status of the high-speed radio frequency (RF) switches are periodically controlled to modulate the static excitation amplitude of the TMA elements. Thus, an additional degree of freedom, namely 'time' is invoked to produce the desired time-averaged low sidelobe level (SLL) pattern at the operating carrier frequency [4, 5]. At the same time, the harmonics caused by the time-periodic pulse modulation are explored to produce multiple harmonic patterns [6, 7], and the same have been beneficially exploited in different communication systems [8–11]. The sideband radiations (SRs) as obtained in TMA are also found to be useful in various smart antenna based applications, like cognitive radio [12], radar [13, 14], multiple-input-multiple-output [15], digital communication [16], and physical layer security [17]. However, for uniform period TMA (UTMA), because of utilizing unique frequency of the modulating pulse, the harmonics from the individual array elements are accumulated while, for nonuniform period TMA (NTMA), due to the distinct modulation frequency, the produced harmonics from the individual array elements are distributed in the space at different frequencies [18–20]. Thus, compared to UTMA, NTMA is worthy of offering the same centre frequency pattern with significantly suppressed sideband level (SBL) [21, 22]. Elsewhere, different time-modulation strategies such as variable aperture size (VAS) [4], pulse-shifting [23], pulse splitting [24–26], pattern multiplication [27], and quantized aperture size (QAS) [28] with adoption of various metaheuristic optimization algorithms [25, 29–32] have been extensively used to synthesize the desired centre frequency pattern by simultaneously suppressing sideband radiation. Toward this, some hardware-based methods are also employed. For example, a 3 dB power divider [33] and a modified switching sequences with limited bandwidth of the antenna

Received 11 September 2022, Accepted 11 January 2023, Scheduled 27 January 2023

* Corresponding author: Sujoy Mandal (sujoymndl2@gmail.com).

The authors are with the Microwave and Antenna Research Laboratory, Department of E.C.E, National Institute of Technology, Durgapur, Durgapur-713209, India.

elements [34] are introduced. In other approaches, evolutionary algorithm is used along with array thinning to increase the directivity of time-modulated planar array [35]. Simultaneously, several closed-form mathematical expressions to calculate the total sideband power (P_{SR}) of various antenna array geometries such as linear [36, 37], planar [38], and geometry independent ones [39] are reported, and the formulations are further extended by considering different types of the modulating pulses [40, 41] and element patterns [42]. Meanwhile, some approaches for calculating the total sideband power (P_{SR}) of NTMA are also reported [43–45]. In [43], an expression is derived for the modulation frequencies with prime coefficients, while in [44], by classifying two categories of NTMA, specifically, non-degenerate NTMA (ND-NTMA) and degenerate NTMA (D-NTMA), the corresponding P_{SR} expressions are derived. For the arbitrarily selected modulation frequency, a P_{SR} expression is also obtained in [45]. Moreover, by investigating the effect of multipath characteristics by placing the array above a specific height of a conductive ground plane, the P_{SR} expressions for both UTMA [46] and NTMA [47] are reported. However, in the above formulations of NTMA in [43–45], the pulse shifting effect of time-modulation is not considered. With respect to other time-modulation approaches, the major advantage of using the pulse shifting strategy is to achieve almost time-independent power patterns with reduced P_{SR} [48].

In this paper, considering universal omnidirectional element pattern in the form of $\sin^a\theta\,|\cos\theta|^b$, $a > -1$, $b > -1/2$, the generalized P_{SR} expression of the NTMAs with pulse-shifted modulation is presented for the linear, planar, and volumetric array geometries. Usually, the expression for the sideband power is obtained in terms of hyper geometric function for which long computation time is required. Therefore, the derived expressions of different array geometries with various element patterns are formulated in simplified forms without hypergeometric function with the objective for the time-efficient computation of the percentage of sideband power loss ($P_{SR}^{\%}$). Representative numerical results are presented to show the effectiveness of using the obtained simplified expressions to accurately calculate P_{SR} with significantly less time than the numerical integration method. The remaining part of this paper is arranged as follows. The mathematical derivations are carried out in Section 2. Through numerical results and analysis, the efficiency of using the proposed simplified expressions is demonstrated in Section 3. Finally, in Section 4, the concluding remarks are drawn.

2. MATHEMATICAL FORMULATION

Let us consider an arbitrarily shaped volumetric NTMA consisting of N number of elements arranged in the three-dimensional (XYZ) Cartesian coordinate system. The array elements dealing with carrier signal of frequency, f_0, are modulated using periodic rectangular pulses with the modulation frequency $f_n : \forall n \in [1, N]$. For volumetric NTMA, the array factor expression can be obtained as [42],

$$AF(\theta,\phi,t) = e^{j2\pi f_0 t}\sum_{n=1}^{N} V_n C_{n0} e^{j\alpha_n}\cdot e^{j\beta(\vec{R}_n\cdot\vec{r})} + \sum_{n=1}^{N}\sum_{\substack{k=-\infty,\\ k\neq 0}}^{\infty} V_n C_{nk} e^{j2\pi(f_0+kf_n)t} e^{j\alpha_n}\cdot e^{j\beta(\vec{R}_n\cdot\vec{r})}. \quad (1)$$

where V_n and α_n denote the static excitation amplitude and phase of the n^{th} element, and β represents the wavenumber of the background medium. $\vec{R}_n$ and $\vec{r}$ are the position and unit direction cosine vector in spherical coordinate system, and are expressed as

$$\vec{R}_n = R_{x_n}\hat{i} + R_{y_n}\hat{j} + R_{z_n}\hat{k} \quad (2)$$

$$\vec{r} = \sin\theta\cos\phi\hat{i} + \sin\theta\sin\phi\hat{j} + \cos\theta\hat{k} \quad (3)$$

where R_{x_n}, R_{y_n}, and R_{z_n} represent the position of the element on X, Y, and Z axes, respectively. In (1), C_{nk} represents the Fourier coefficient of n^{th} element at the k^{th} harmonic. For time-modulation with pulse shifting strategy using periodic switching function $U_n(t)$ as depicted in Fig. 1, it can be given as [23],

$$C_{nk} = \begin{cases} f_n\left(\tau_n^{off} - \tau_n^{on}\right); & \text{for } k = 0 \\ \dfrac{\sin\left[\pi k f_n\left(\tau_n^{off} - \tau_n^{on}\right)\right]}{\pi k} e^{-j\pi k f_n\left(\tau_n^{off}+\tau_n^{on}\right)}; & \text{for } k \neq 0. \end{cases} \quad (4)$$

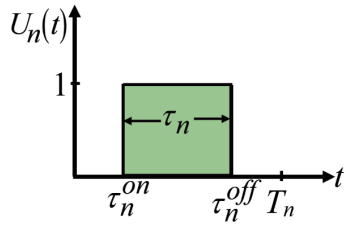

Figure 1. Schematic representation of pulse-shift switching strategy.

where τ_n^{on} and τ_n^{off} denote the periodic switch '*on*' and '*off*' time instant of the n^{th} element over a complete pulse period, $T_n = 1/f_n$.

According to pattern multiplication, the total field ($E(\theta, \phi, t)$) radiated by the array with individual element pattern ($e(\theta, \phi)$) can be obtained as

$$E(\theta, \phi, t) = e(\theta, \phi)\, AF(\theta, \phi, t). \tag{5}$$

For the universal omnidirectional element pattern in ϕ plane, $e(\theta, \phi)$ is expressed as [42]

$$e(\theta, \phi) = \sin^a \theta \left|\cos\theta\right|^b, \quad a > -1,\ b > -1/2 \tag{6}$$

Combining (1), (4), (5), and (6), the expression of resultant array field pattern can be written as

$$E(\theta, \phi, t) = \sin^a \theta \left|\cos\theta\right|^b \left[e^{j2\pi f_0 t} \sum_{n=1}^{N} V_n C_{n0} e^{j\alpha_n} \cdot e^{j\beta(\vec{R}_n \cdot \vec{r})} + \sum_{n=1}^{N} \sum_{\substack{k=-\infty, \\ k\neq 0}}^{\infty} V_n C_{nk} e^{j2\pi(f_0 + kf_n)t} e^{j\alpha_n} \cdot e^{j\beta(\vec{R}_n \cdot \vec{r})} \right] \tag{7}$$

For UTMA, elements are modulated with the unique modulation frequency, say, f_m, i.e., $f_1 = f_2 = \ldots = f_N = f_m$. Thus, at k^{th} harmonic, the radiated signals from all elements are overlapped at the same frequency, $f_k = f_0 \pm kf_m$ and accumulated in the space as can be observed from (7). For NTMA, the modulation frequencies of the elements are different, i.e., $f_1 \neq f_2 \neq \ldots \neq f_N$. Thus, the radiations from the elements at a particular k^{th} harmonic order are generated at different frequencies $f_{nk} = f_0 + kf_n$. Despite different modulation frequencies in NTMA, at a specific k^{th} order harmonic signal frequency of one element (say, the n^{th}) may be equal to the q^{th} order harmonic of another element (say, m^{th}). Thus, based on radiated signal frequency in NTMA, some harmonic components are overlapping, and some are non-overlapping in space. As an outcome, NTMA is classified as non-degenerate NTMA (ND-NTMA) and degenerate NTMA (D-NTMA) as detailed in [44]. It can be seen from the first part of (7), though the array elements are modulated with different modulation frequencies, the fundamental component of the field radiated by the individual elements appears at the same frequency and is added in the space at f_0. Therefore, by exploiting the fundamental component of the Fourier coefficient C_{n0}, the desired power pattern at f_0 can be synthesized. Now, for the pulse-shifted switching strategy considering the harmonic components of the elements as indicated by second part of (7), the mathematical formulations of sideband power (P_{SR}) of both NTMA types are carried out in the subsequent sections.

2.1. Sideband Power of Pulse-Shifted ND-NTMA

For ND-NTMA, all possible harmonic signals of the time-modulated elements appear at different frequencies: $f_{nk} \neq f_{mq} : \forall(n, m) \in [1, N] \& (n \neq m)$ and $\forall(k, q) \in [-\infty, +\infty] \& (k \neq q \neq 0)$. Hence, individual harmonic radiation from different array elements becomes various sideband radiation of the array. So, power radiated by the n^{th} element at the k^{th} harmonic can be obtained as [44]

$$p_{nk} = \frac{1}{2} \int_0^{2\pi} \int_0^{\pi} \sin^{2a}\theta \left|\cos\theta\right|^{2b} |V_n|^2 |C_{nk}|^2 \sin\theta d\theta d\phi$$

$$= \pi |V_n|^2 |C_{nk}|^2 \int_0^{\pi} \sin^{2a+1}\theta \, |\cos\theta|^{2b} d\theta \tag{8}$$

Substituting the expression of C_{nk} from (4) and simplifying the integration, Equation (8) is reduced to

$$p_{nk} = \pi |V_n|^2 \frac{\sin^2[\pi k \varsigma_n]}{(\pi k)^2} B(a+1, b+1/2) \tag{9}$$

where $B(\cdot)$ represents the beta function, and ς_n is normalized on time duration, given as $\varsigma_n = \varsigma_n^{off} - \varsigma_n^{on}$ with $\varsigma_n^{on} = f_n \tau_n^{on}$ and $\varsigma_n^{off} = f_n \tau_n^{off}$ being the normalized '*on*' and '*off*' time instant of the n^{th} element. Considering all the harmonics, the total power radiated by n^{th} array element is obtained as

$$P_n = \sum_{\substack{k=-\infty, \\ k\neq 0}}^{\infty} p_{nk} = \pi |V_n|^2 \int_0^{\pi} \sin^{2a+1}\theta \, |\cos\theta|^{2b} \theta d\theta \sum_{\substack{k=-\infty, \\ k\neq 0}}^{\infty} \frac{\sin^2[\pi k \varsigma_n]}{(\pi k)^2} \tag{10a}$$

$$= \pi |V_n|^2 B(a+1, b+1/2) \sum_{\substack{k=-\infty, \\ k\neq 0}}^{\infty} \frac{\sin^2[\pi k \varsigma_n]}{(\pi k)^2} \tag{10b}$$

Thus, by taking into account of all the array elements, the total sideband power of pulse-shifted ND-NTMA (P_{SR}^{ND}) can be obtained from (10(b)), and after following the simplification steps as detailed in [44], it is expressed as

$$P_{SR}^{ND} = \sum_{n=1}^{N} P_n = \pi \sum_{n=1}^{N} |V_n|^2 \varsigma_n (1-\varsigma_n) B(a+1, b+1/2). \tag{11}$$

As a special case of the element pattern with $a = b = 0$ in (6), $e(\theta, \phi)$ becomes isotropic one ($e(\theta, \phi) = 1$), and the corresponding expression in (11) is reduced to take the same form as that without pulse-shifted ND-NTMA in [44] and given as

$$P_{SR}^{ND}|_{iso} = 2\pi \sum_{n=1}^{N} V_n^2 \varsigma_n (1-\varsigma_n) \tag{12}$$

2.2. Sideband Power of Pulse-Shifted D-NTMA

In D-NTMA, certain harmonic signals may overlap with the harmonics from some other array elements. Let us consider an example of D-NTMA, the *(ik)*th harmonics of the n^{th} element overlap with the *(iq)*th harmonics of the m^{th} element, where 'i' is any natural number. Let us further assume that χ_{ov} is the set of elements from which the radiated harmonic signals are overlapped, and ρ_n is the first overlapping harmonic index of the n^{th} element. So, the sideband pattern generated for all the overlapping harmonics belonging to the χ_{ov} set of elements would become

$$E_{\chi_{ov}}^{D}(\theta, \phi, t) = \sin^a\theta \, |\cos\theta|^b \sum_{\substack{k=-\infty, \\ k\neq 0, \\ k=i\rho_n}}^{\infty} \left[\sum_{n\in\chi_{ov}} V_n C_{nk} e^{j2\pi(f_0+kf_n)t} e^{j\alpha_n} \cdot e^{j\beta(\vec{R}_n \cdot \vec{r})} \right]. \tag{13}$$

Hence, at $k = i\rho_n^{th}$ overlapping harmonics, the power radiated by the χ_{ov} set of elements can be obtained as [44]

$$P_{\chi_{ov} i\rho_n} = \frac{1}{2} \int_0^{2\pi} \int_0^{\pi} \sin^{2a}\theta \cos^{2b}\theta \left[\sum_{n\in\chi_{ov}} (|V_n| \, |C_{ni\rho_n}|)^2 + \sum_{\substack{n,m\in\chi_{ov}, \\ n\neq m}} V_n V_m^* C_{ni\rho_n} C_{mi\rho_m}^* e^{j\alpha_{nm}} \cdot e^{j\beta(\vec{R}_{nm}\vec{r})} \right] \sin\theta d\theta d\phi. \tag{14}$$

where $\alpha_{nm} = \alpha_n - \alpha_m$, and $\vec{R}_{nm} = R_{x_{nm}}\hat{i} + R_{y_{nm}}\hat{j} + R_{z_{nm}}\hat{k}$. $R_{x_{nm}} = |R_{x_n} - R_{x_m}|$, $R_{y_{nm}} = |R_{y_n} - R_{y_m}|$ and $R_{z_{nm}} = |R_{z_n} - R_{z_m}|$ represent the respective inter-element distances.

Considering all the overlapping harmonics the total radiated power corresponding to the χ_{ov} set of elements can be obtained as

$$P_{\chi_{ov}} = \underbrace{\frac{1}{2}\sum_{n\in\chi_{ov}}\sum_{\substack{i=-\infty,\\ i\neq 0}}^{\infty}\left[|V_n|^2\cdot|C_{ni\rho_n}|^2\int_0^{2\pi}\int_0^{\pi}\sin^{2a+1}\theta\cos^{2b}\theta d\theta d\phi\right]}_{I_1}$$
$$+\underbrace{\frac{1}{2}\sum_{\substack{n,m\in\chi_{ov},\\ n\neq m}}\sum_{\substack{i=-\infty,\\ i\neq 0}}^{\infty}\left[V_nV_m^*C_{ni\rho_n}C_{mi\rho_m}^*\int_0^{2\pi}\int_0^{\pi}\sin^{2a+1}\theta\cos^{2b}\theta e^{j\alpha_{nm}}\cdot e^{j\beta(\vec{R}_{nm}\cdot\vec{r})}d\theta d\phi\right]}_{I_2}$$
$$= I_1 + I_2 \tag{15}$$

Here, I_1 and I_2 are defined as follows.

$$I_1 = \pi\sum_{n\in\chi_{ov}}\sum_{\substack{i=-\infty,\\ i\neq 0}}^{\infty}\left[|V_n|^2.|C_{ni\rho_n}|^2\int_0^{\pi}\sin^{2a+1}\theta\cos^{2b}\theta d\theta\right] \tag{16a}$$

$$= \pi\sum_{n\in\chi_{ov}}|V_n|^2\left\{\sum_{\substack{i=-\infty,\\ i\neq 0}}^{\infty}C_{ni\rho_n}^2\right\}B(a+1,b+1/2) \tag{16b}$$

Simplifying the summation of $\sum\limits_{\substack{i=-\infty,\\ i\neq 0}}^{\infty}C_{ni\rho_n}^2$ as in [44], the integration I_1 can be obtained as,

$$I_1 = \pi B(a+1,b+1/2)\sum_{n\in\chi_{ov}}\frac{|V_n|^2}{\rho_n}\varsigma_n(1-\rho_n\varsigma_n) \tag{17}$$

The infinite summation of the Fourier coefficients, $\sum\limits_{\substack{i=-\infty,\\ i\neq 0}}^{\infty}C_{ni\rho_n}C_{mi\rho_m}^*$ of I_2 as denoted in (15) can be simplified as [37, 44]

$$\sum_{i=-\infty}^{\infty}C_{ni\rho_n}C_{mi\rho_m}^* = \frac{1}{\rho_m\rho_n}\left[\overline{\varsigma_{\rho_m\rho_n}} - \rho_m\rho_n\varsigma_m\varsigma_n\right]. \tag{18}$$

where $\overline{\varsigma_{\rho_m\rho_n}}$ is the intersected on-time duration of the two elements (m,n) at their overlapping harmonic indexes ρ_m and ρ_n respectively, and can be expressed as

$$\overline{\varsigma_{\rho_m\rho_n}} = \left[\min(\rho_n\varsigma_n^{off},\rho_m\varsigma_m^{off}) - \max(\rho_n\varsigma_n^{on},\rho_m\varsigma_m^{on})\right]. \tag{19}$$

Finally, the expression of I_2 becomes,

$$I_2 = \frac{1}{2}\sum_{\substack{n,m\in\chi_{ov},\\ n\neq m}}\left[V_nV_m^*\frac{1}{\rho_m\rho_n}\left[\overline{\varsigma_{\rho_m\rho_n}} - \rho_m\rho_n\varsigma_m\varsigma_n\right]\underbrace{\int_0^{2\pi}\int_0^{\pi}\sin^{2a+1}\theta\cos^{2b}\theta e^{j\alpha_{nm}}\cdot e^{j\beta(\vec{R}_{nm}\cdot\vec{r})}d\theta d\phi}_{I_3}\right] \tag{20}$$

Let us assume the integration in (20) as

$$I_3 = \int_0^{2\pi}\int_0^{\pi} \sin^{2a+1}\theta \cos^{2b}\theta e^{j\alpha_{nm}} \cdot e^{j\beta(\vec{R}_{nm}.\vec{r})} d\theta d\phi \tag{21}$$

This can be simplified as [42]

$$I_3 = 2\pi \sum_{s=0}^{\infty} \frac{(\beta R_{z_{nm}})^{2s}}{(2s)!} B\left(a+1, b+s+1/2\right) \times {}_1F_2\left(\begin{array}{c} a+1 \\ 1, a+b+s+3/2 \end{array} \middle| -\left(\frac{\beta\psi_{R_{nm}}}{2}\right)^2 \right) \tag{22}$$

The summation in (22) represents the Maclaurin series expansion of order 's', where ${}_1F_2\left(.\right)$ represents the hyper-geometric function [49, 50]; $\psi_{R_{nm}}$ and $R_{z_{nm}}$ are the inter-element distance between the n^{th} and m^{th} element in the XY plane and along Z-axis, and are given as $\psi_{R_{nm}} = \sqrt{(R_{x_n} - R_{x_m})^2 + (R_{y_n} - R_{y_m})^2}$ and $R_{z_{nm}} = \sqrt{(R_{z_n} - R_{z_m})^2}$.

Using (17), (20), and (22), the expression of $P_{\chi_{ov}}$ in (15) can be obtained as

$$\begin{aligned} P_{\chi_{ov}} \;=\; & \pi B\left(a+1, b+1/2\right) \sum_{n\in\chi_{ov}} \frac{|V_n|^2}{\rho_n} \varsigma_n \left(1 - \rho_n \varsigma_n\right) \\ & + \frac{1}{2} \sum_{\substack{n,m\in\chi_{ov,} \\ n\neq m}} V_n V_m^* e^{j\alpha_{nm}} \left[\frac{1}{\rho_m \rho_n} \left[\overline{\varsigma_{\rho_m\rho_n}} - \rho_m\rho_n\varsigma_m\varsigma_n\right] \times I_3 \right] \end{aligned} \tag{23a}$$

Assuming that all possible sets of elements that can produce different infinite series of overlapping harmonics as χ, the total sideband power radiated due to all possible overlapping harmonics ($P_{SR}^{D_{ov}}$) is expressed as [44]

$$P_{SR}^{D_{ov}} \;=\; \sum_{\chi_{ov}\in\chi} P_{\chi_{ov}} \tag{23b}$$

Therefore, the P_{SR} of D-NTMA (P_{SR}^{D}) can be obtained as [44]

$$P_{SR}^{D} = P_{SR}^{D_{ov}} + P_{SR}^{D_{ind}} - P_{SR}^{D_{fov}} \tag{24a}$$

where $P_{SR}^{D_{ind}}$ and $P_{SR}^{D_{fov}}$ represent the power obtained from the individual radiation of the infinite harmonics and that from the individual radiation at the overlapping frequencies, respectively. $P_{SR}^{D_{ind}}$ is calculated like P_{SR}^{ND} as mentioned in (10(a))–(11). Considering both overlapping and non-overlapping harmonics as detailed in [44], the expression of P_{SR} for the volumetric D-NTMA (P_{SR}^{D}) can be obtained as

$$\begin{aligned} P_{SR}^{D} \;=\; & \pi B\left(a+1, b+1/2\right) \sum_{n=1}^{N} |V_n|^2 \varsigma_n (1 - \varsigma_n) \\ & + \frac{1}{2} \sum_{\chi_{ov}\in\chi} \sum_{\substack{n,m\in\chi_{ov,} \\ n\neq m}} V_n V_m^* e^{j\alpha_{nm}} \left[\frac{1}{\rho_m \rho_n} \left\{\overline{\varsigma_{\rho_m\rho_n}} - \rho_m\rho_n\varsigma_m\varsigma_n\right\} \times I_3 \right] \end{aligned} \tag{24b}$$

For the array with a large number of antenna elements, the numerical integration (NI) method to calculate P_{SR} by using (15) and (10(a)) with summation over N requires long computation time. For different possible combinations of 'a' and 'b', Equation (24(b)) can be used for calculating the power. However, Equation (24(b)) is associated with the hypergeometric function that needs increased computation time [49]. Therefore, with further simplification of (24(b)), the computation time can be reduced significantly. So, for different element patterns corresponding to the different values of 'a' and 'b', the expression of I_3, as obtained in (22), is further simplified. It is shown that using the simplified expressions without hypergeometric function, time to calculate P_{SR} is significantly reduced. This is

because the calculation of hypergeometric function in (22), as well as in (24(b)), needs significantly more computation time than the simplified expressions as obtained in terms of Beta function, Bessel's function, or Gamma function.

For different array geometries having different types of element patterns $e(\theta,\phi)$, the formulated simplified closed form expressions of P_{SR} of D-NTMA are presented in the following subsections.

2.2.1. Volumetric Array

For the volumetric array geometry with different values of 'a' and 'b', the expressions of I_3 are simplified and presented in Table 1. Here, $J(\cdot)$ represents the Bessels function, while $\Gamma(\cdot)$ represents the Gamma function. Thus for different types of element patterns, using the simplified expression of I_3 in (24.1)–(24.9) the corresponding expressions for the sideband power can be obtained from (24(b)). For reference, the expression of P_{SR} with isotropic element pattern $e(\theta,\phi)=1$ is derived as follows. For isotropic pattern, $a=0$, $b=0$, and $B(1,1/2)=2$. Considering $s=0$, the expression of I_3 is simplified [42] and expressed in (24.1). Here, d_{mn} represents the inter-element distances of the array. Therefore, P_{SR}^{D} is obtained from (24(b)) as

$$P_{SR}^{D}\big|_{iso}=2\pi\varsigma_n\sum_{n=1}^{N}|V_n|^2(1-\varsigma_n)+\frac{1}{2}\sum_{\substack{n,m\in\chi_{ov},\\ n\neq m}}V_nV_m^{*}\frac{1}{\rho_m\rho_n}[\overline{\varsigma_{\rho_m\rho_n}}-\rho_m\rho_n\varsigma_m\varsigma_n]4\pi\sin c(\beta d_{mn})e^{j\alpha_{nm}} \quad (25)$$

Similarly for linear and planar array geometries the simplified generalized expression of P_{SR}^{D} can be derived as follows.

2.2.2. Planar Array

Let us consider that the array is placed in the XY plane. For such a planar array, $R_{z_{nm}}=0$. So, the simplified form of I_3 is obtained from (22) as

$$I_3=2\pi B(a+1,b+1/2)\,{}_1F_2\left(\begin{array}{c|c} a+1 & \\ 1,a+b+3/2 & -\left(\frac{\beta\psi_{R_{nm}}}{2}\right)^2\end{array}\right) \quad . \quad (26)$$

Therefore, using (26) in (24(b)), the expression of P_{SR}^{D} in the XY plane can be obtained. However, the resultant expression of P_{SR}^{D} consists of an increased computational time based hypergeometric function. To reduce the computation time of the resultant expression corresponding to the different element patterns having different values of 'a' and 'b', I_3 in (26) is further simplified and presented in (26.1)–(26.9), Table 2.

Now, for a special case, let us consider the planar array of element pattern without having any *sin* term, i.e., the element pattern is of the form $e(\theta,\phi)=\cos^{b}\theta$. For this case, the simplified expression of I_3 is written as,

$$I_3=4\pi 2^{b-1/2}\Gamma(b+1/2)\frac{J_{b+1/2}(\beta\psi_{R_{nm}})}{(\beta\psi_{R_{nm}})^{b+1/2}}. \quad (27)$$

Thus, I_3 is obtained in terms of the Bessel function and Gamma function. Using (27) in (24(b)), the final expression can be calculated without computation of the hypergeometric function.

2.2.3. Linear Array

Let the antenna array placed along the Z-axis. In this scenario $\psi_{R_{nm}}=0$. So, the expression of I_3 can be written from (21) as

$$I_3=e^{j\alpha_{nm}}\int_0^{\pi}\sin^{2a+1}\theta\cos^{2b}\theta e^{j\beta R_{z_{nm}}\cos\theta}d\theta \quad (28)$$

Table 1. Simplified expressions of I_3 for the volumetric array of various types of element pattern with different values of (a, b).

Sl. No.	*(a, b)*	I_3	Eq. No.
1.	a=0, b=0	$4\pi\,\mathrm{sinc}\left(\beta d_{nm}\right);\quad d_{nm}=\sqrt{\psi^{2}_{R_{nm}}+R^{2}_{z_{nm}}}$ with $s=0$ $\dfrac{\Gamma(s+3/2)J_{s+1/2}\left(2\beta^{2}\psi^{2}_{R_{nm}}\right)^{1/2}}{\left(2\beta^{2}\psi^{2}_{R_{nm}}\right)^{(s/2+1/4)}}$ with $s\neq 0$	(24.1)
2.	a=0.5, b=0	${}_1F_2\left(\begin{matrix}1\\ 3/2,\ s+2\end{matrix}\middle\vert -\left(\dfrac{\beta\psi_{R_{nm}}}{2}\right)^{2}\right)$	(24.2)
3.	a=1, b=0	$\dfrac{\Gamma(s+5/2)J_{s+3/2}\left(2\left(\dfrac{\beta^{2}\psi^{2}_{R_{nm}}}{4}\right)^{1/2}\right)}{\left(\dfrac{\beta^{2}\psi^{2}_{R_{nm}}}{4}\right)^{(s/2+3/4)}}-\dfrac{\beta^{2}\psi^{2}_{R_{nm}}\Gamma(s+7/2)J_{s+5/2}\left(2\left(\dfrac{\beta^{2}\psi^{2}_{R_{nm}}}{4}\right)^{1/2}\right)}{4(s+5/2)\left(\dfrac{\beta^{2}\psi^{2}_{R_{nm}}}{4}\right)^{(s/2+5/4)}}$	(24.3)
4.	a=0, b=0.5	$\dfrac{\Gamma(s+2)J_{s+1}\left(2\left(\dfrac{\beta^{2}\psi^{2}_{R_{nm}}}{4}\right)^{1/2}\right)}{\left(\dfrac{\beta^{2}\psi^{2}_{R_{nm}}}{4}\right)^{(s/2+1/2)}}$	(24.4)
5.	a=0.5, b=0.5	${}_1F_2\left(\begin{matrix}1\\ 3/2,\ s+5/2\end{matrix}\middle\vert -\left(\dfrac{\beta\psi_{R_{nm}}}{2}\right)^{2}\right)$	(24.5)
6.	a=1, b=0.5	$\dfrac{\Gamma(s+3)J_{s+2}\left(2\left(\dfrac{\beta^{2}\psi^{2}_{R_{nm}}}{4}\right)^{1/2}\right)}{\left(\dfrac{\beta^{2}\psi^{2}_{R_{nm}}}{4}\right)^{(s/2+1)}}-\dfrac{\beta^{2}\psi^{2}_{R_{nm}}\Gamma(s+4)J_{s+3}\left(2\left(\dfrac{\beta^{2}\psi^{2}_{R_{nm}}}{4}\right)^{1/2}\right)}{4(s+3)\left(\dfrac{\beta^{2}\psi^{2}_{R_{nm}}}{4}\right)^{(s/2+3/2)}}$	(24.6)
7.	a=0, b=1	$\dfrac{\Gamma(s+5/2)J_{s+3/2}\left(2\left(\dfrac{\beta^{2}\psi^{2}_{R_{nm}}}{4}\right)^{1/2}\right)}{\left(\dfrac{\beta^{2}\psi^{2}_{R_{nm}}}{4}\right)^{(s/2+3/4)}}$	(24.7)
8.	a=0.5, b=1	${}_1F_2\left(\begin{matrix}1\\ 3/2,\ s+3\end{matrix}\middle\vert -\left(\dfrac{\beta\psi_{R_{nm}}}{2}\right)^{2}\right)$	(24.8)
9.	a=1, b=1	$\dfrac{\Gamma(s+7/2)J_{s+5/2}\left(2\left(\dfrac{\beta^{2}\psi^{2}_{R_{nm}}}{4}\right)^{1/2}\right)}{\left(\dfrac{\beta^{2}\psi^{2}_{R_{nm}}}{4}\right)^{(s/2+5/4)}}-\dfrac{\beta^{2}\psi^{2}_{R_{nm}}\Gamma(s+9/2)J_{s+7/2}\left(2\left(\dfrac{\beta^{2}\psi^{2}_{R_{nm}}}{4}\right)^{1/2}\right)}{4(s+7/2)\left(\dfrac{\beta^{2}\psi^{2}_{R_{nm}}}{4}\right)^{(s/2+7/4)}}$	(24.9)

Table 2. Simplified expressions of I_3 for various values of (a, b) for planar NTMA placed in XY plane.

Sl. No.	(a, b)	I_3	Eq. No.
1.	a=0, b=0	$\frac{\sin\left(\beta\psi_{R_{nm}}\right)}{\beta\psi_{R_{nm}}}$	(26.1)
2.	a=0.5, b=0	$\left\{J_0\left(\frac{-\beta^2\psi_{R_{nm}}^2}{4}\right)^{1/2}\right\}^2+\left\{J_1\left(\frac{-\beta^2\psi_{R_{nm}}^2}{4}\right)^{1/2}\right\}^2$	(26.2)
3.	a=1, b=0	$\frac{3\beta^2\psi_{R_{nm}}^2\sin\left(\beta\psi R_{nm}\right)-\sin\left(\beta\psi R_{nm}\right)+\beta\psi R_{nm}\cos\left(\beta\psi R_{nm}\right)}{2\left(\beta\psi_{R_{nm}}\right)^3}$	(26.3)
4.	a=0, b=0.5	$\frac{2J_1\left(\beta\psi_{R_{nm}}\right)}{\beta\psi_{R_{nm}}}$	(26.4)
5.	a=0.5, b=0.5	${}_1F_2\left(3/2,\ 5/2\middle\vert -\left(\frac{\beta\psi_{R_{nm}}}{2}\right)^2\right)$	(26.5)
6.	a=1, b=0.5	$8\frac{J_0\left(\beta\psi_{R_{nm}}\right)}{\left(\beta\psi_{R_{nm}}\right)^2}+\frac{\left(4\beta^2\psi_{R_{nm}}^2-16\right)J_1\left(\beta\psi_{R_{nm}}\right)}{\left(\beta\psi_{R_{nm}}\right)^3}$	(26.6)
7.	a=0, b=1	$\frac{3\sin\left(\beta\psi_{R_{nm}}\right)-3\beta\psi_{R_{nm}}\cos\left(\beta\psi_{R_{nm}}\right)}{\left(\beta\psi_{R_{nm}}\right)^3}$	(26.7)
8.	a=0.5, b=1	$\frac{16\left\{J_1\left(\frac{-\beta^2\psi_{R_{nm}}^2}{4}\right)^{1/2}\right\}^2}{\left(\beta\psi_{R_{nm}}\right)^2}-\frac{16J_0\left(\frac{-\beta^2\psi_{R_{nm}}^2}{4}\right)^{1/2}J_1\left(\frac{-\beta^2\psi_{R_{nm}}^2}{4}\right)^{1/2}\left(\frac{-\beta^2\psi_{R_{nm}}^2}{4}\right)^{1/2}}{\left(\beta\psi_{R_{nm}}\right)^2}$	(26.8)
9.	a=1, b=1	$\frac{-15\left\{9\sin\left(\beta\psi R_{nm}\right)+\beta^3\psi_{R_{nm}}^3\cos\left(\beta\psi R_{nm}\right)-4\beta^2\psi_{R_{nm}}^2\sin\left(\beta\psi R_{nm}\right)-9\beta\psi R_{nm}\cos\left(\beta\psi R_{nm}\right)\right\}}{2\left(\beta\psi_{R_{nm}}\right)^5}$	(26.9)

This expression can be simplified as [51]

$$I_3 = B\left(a+1, b+1/2\right){}_1F_2\left(\begin{array}{c} b+1/2 \\ 1/2, a+b+3/2 \end{array}\middle| -\left(\frac{\beta R_{z_{nm}}}{2}\right)^2\right) \tag{29}$$

where, $R_{z_{nm}} = \sqrt{\left(R_{z_n} - R_{z_m}\right)^2}$.

Thus, for the array lying along the Z-axis, P_{SR}^D can be obtained by putting (29) in (24(b)). However, like volumetric and planar arrays, the expression is involved with hypergenmetric function. So, similar to (24) and (26), for different element patterns the expression of I_3 in (29) is simplified and given in Table 3, (29.1)–(29.9).

Table 3. Simplified expressions of I_3 for various values of (a, b) of linear NTMA placed along Z-axis.

Sl. No.	*(a, b)*	I_3	Eq. No.
1.	*a=0, b=0*	$\frac{\sin(\beta R_{z_{nm}})}{\beta R_{z_{nm}}}$	(29.1)
2.	*a=0.5, b=0*	$\frac{2J_1 \sin(\beta R_{z_{nm}})}{\beta R_{z_{nm}}}$	(29.2)
3.	*a=1, b=0*	$\frac{3\sin\left(\beta R_{z_{nm}}\right) - 3\beta R_{z_{nm}} \cos\left(\beta R_{z_{nm}}\right)}{\beta R_{z_{nm}}}$	(29.3)
4.	*a=0, b=0.5*	$\frac{2\sinh\left(-\beta^2 R_{z_{nm}}^2\right)^{1/2}\left(-\beta^2 R_{z_{nm}}^2\right)^{3/2} - \beta^2 R_{z_{nm}}^2 + \beta^2 R_{z_{nm}}^2 \cosh\left(-\beta^2 R_{z_{nm}}^2\right)^{1/2}}{\left(\beta R_{z_{nm}}\right)^4}$	(29.4)
5.	*a=0.5, b=0.5*	${}_1F_2\left(1/2, {}^{1}_{5/2} \middle| -\left(\frac{\beta R_{z_{nm}}}{2}\right)^2\right)$	(29.5)
6.	*a=1, b=0.5*	$\frac{-12\left(2\cosh\left(-\frac{\beta^2 R_{z_{nm}}^2}{4}\right)^{1/2} - \sinh\left(-\frac{\beta^2 R_{z_{nm}}^2}{4}\right)^{1/2} \Big/ \left(-\frac{\beta^2 R_{z_{nm}}^2}{4}\right)^{1/2}\right)^2}{\left(-\frac{\beta^2 R_{z_{nm}}^2}{4}\right)^{1/2}} - \frac{4\sinh\left(\left(-\frac{\beta^2 R_{z_{nm}}^2}{4}\right)^{1/2}\right)^2}{\left(\beta R_{z_{nm}}\right)^2}$	(29.6)
7.	*a=0, b=1*	$\frac{\cosh\left(-\beta^2 R_{z_{nm}}^2\right)^{1/2}\left(-\beta^2 R_{z_{nm}}^2\right)^{1/2} - 6\sinh\left(-\beta^2 R_{z_{nm}}^2\right)^{1/2} + 3\beta^2 R_{z_{nm}}^2 \sinh\left(-\beta^2 R_{z_{nm}}^2\right)^{1/2}}{\left(-\beta^2 R_{z_{nm}}^2\right)^{3/2}}$	(29.7)
8.	*a=0.5, b=1*	$\frac{24J_0\left(\beta R_{z_{nm}}\right)}{\left(\beta R_{z_{nm}}\right)^2} + 8\frac{\left(\beta^2 R_{z_{nm}}^2 - 6\right)J_1\left(\beta R_{z_{nm}}\right)}{\left(\beta R_{z_{nm}}\right)^3}$	(29.8)
9.	*a=1, b=1*	$\frac{-15\left\{12\sin\left(\beta R_{z_{nm}}\right) + \left(\beta R_{z_{nm}}\right)^3 \cos\left(\beta R_{z_{nm}}\right)^{1/2} - 5\left(\beta R_{z_{nm}}\right)^2 \sin\left(\beta R_{z_{nm}}\right) - 12\,\beta R_{z_{nm}} \cos\left(\beta R_{z_{nm}}\right)\right\}}{\left(\beta R_{z_{nm}}\right)^5}$	(29.9)

3. NUMERICAL EXAMPLE

In this section, the effectiveness of the obtained simplified expressions in calculating the sideband power loss accurately with less computation time have been demonstrated. In this regard, the derived expressions are used to calculate the power losses associated with linear, planar, and volumetric arrays,

and the obtained results are compared in terms of the accuracy and computation time.

The efficient computation ability of the derived simplified expressions is demonstrated for three types of the array geometries, like — linear, planar, and volumetric arrays. For a particular array geometry, the sideband power losses of both types of NTMAs — ND-NTMA and D-NTMA are calculated in two ways — by means of simplified expressions (SE) and with use of the numerical integration (NI) method. For different element patterns of the respective array geometry, the obtained values of the power losses and the time taken to compute the results are compared. The modulation frequencies of the array elements are selected as $f_n = f_1 \pm (n-1)\Delta f$, where f_1 is the modulation frequency of the first element, and Δf is the change in frequency step of the consecutive elements. For ND-NTMA, f_1 and Δf are taken as (30 MHz, 0.5 MHz) while for D-NTMA these are (2 MHz, 1 MHz), respectively. For all the following examples, the numerical integration is used with the step size of the angular sample of 0.01°.

3.1. Linear Array

Let us assume a linear array of 25 elements placed along the Z-axis. The locations of the array elements are selected randomly as mentioned in Table 4, while the element excitations are selected the same as in [42]. For the arrays with different element types, the NI is used as follows. For ND-NTMA, at first, the power at a particular harmonic of the individual element, p_{nk}, is calculated using the integral in (8). Then, the total harmonic power of the individual element, P_n, is calculated using the infinite series summation in (10(a)), and finally, P_{SR} is obtained with the summation of P_n over the total number of elements N as in (11). For D-NTMA, determining the integrals in (15) and (10(a)) with summation over N, it is calculated from (23(b)) and (24(a)).

Table 4. Locations of the antenna elements in the Z-axis.

Element No.	1	2	3	4	5	6	7	8	9	10	11	12	13
$(z_n) \cdot \lambda$	0.64	0.37	0.81	0.53	0.35	0.94	0.87	0.55	0.62	0.58	0.20	0.3	0.47
Element No.	14	15	16	17	18	19	20	21	22	23	24	25	---
$(zn) \cdot \lambda$	0.23	0.84	0.19	0.22	0.17	0.22	0.43	0.31	0.92	0.43	0.18	0.90	---

Without integration, to directly compute the power losses, the derived simplified expression in (11) is used for ND-NTMA. However, for D-NTMA, first, I_3 is obtained from the derived expression with hypergeometric function in (29) as well as its simplified expressions according to the different values of 'a' and 'b' as in (29.1)–(29.9), and then these are used in (24(b)).

After obtaining the value of P_{SR}, the percentage of sideband power loss ($P_{SR}^{\%}$) is calculated by [44]. The obtained results are mentioned in Table 5. It can be observed that compared to NI, with the error about less than 10^{-14}, the derived expressions corresponding to ND-NTMA and D-NTMA take significantly less time to compute the power. However, for the element pattern with $a = b = 0.5$, the computation time is somewhat higher due to the presence of the hypergeometric function in (29.5). Another point needs to be mentioned here that for a fixed value of 'b', with increasing 'a', $P_{SR}^{\%}$ is decreased, and for a fixed value of 'a', with increasing 'b', $P_{SR}^{\%}$ is increased. This indicates that compared to the isotropic array, power loss for the array with broadside directive element pattern is more.

3.2. Planar Array

To show the computational proficiency of the derived expressions for the planar array, let us consider the same array configuration as in [42]. Similar to linear array, P_{SR} of ND-NTMA is calculated by using NI and the derived expressions. However, for D-NTMA, to compute the power with NI, first, I_3 and I_1 are obtained by using integral in (21) and (16(a)), and for the power due to the individual radiation of the harmonics using the integral equation of (10(a)) with summation over N, and then P_{SR} from (23(b)), (24(a)). The P_{SR} of D-NTMA is also calculated by using the derived expressions (26)

Table 5. Obtained values of $P_{SR}^{\%}$ and corresponding computation time for linear NTMAs for different possible combinations of (a, b) of $e(\theta, \phi)$ (Intel Core i5-4690 CPU @ 3.50 GHz, RAM: 4 GB).

Sl No.	(a, b)	P_{SR}%						Computation time (sec)			
		ND-NTMA			D-NTMA			ND-NTMA		D-NTMA	
		NI	SE	Error	NI	SE	Error	NI	SE	NI	SE Eq. (29.1)-(29.9)
1	(0,0)	4.32	4.32	9.1835e-15	11.16	11.16	3.5120e-14	0.243	0.032	0.222	0.02
2	(0.5,0)	3.78	3.78	5.6205e-16	10.99	10.99	3.8858e-16	0.189	0.015	0.228	0.025
3	(1,0)	3.49	3.49	1.7347e-16	10.9	10.9	2.7062e-15	0.235	0.013	0.219	0.021
4	(0,0.5)	6.33	6.33	2.7188e-14	11.78	11.78	0	0.189	0.015	0.219	0.021
5	(0.5,0.5)	5.23	5.23	2.5229e-15	11.4	11.4	1.295e-14	0.238	24.6	0.222	26.1
6	(1,0.5)	4.62	4.62	4.2313e-14	11.21	11.21	1.144e-15	0.191	0.020	0.228	0.03
7	(0,1)	8.27	8.27	4.3397e-14	12.42	12.42	1.809e-15	0.195	0.032	0.039	0.218
8	(0.5,1)	6.68	6.68	3.8247e-14	11.85	11.85	9.7218e-15	0.219	0.016	0.222	0.025
9	(1,1)	5.77	5.77	2.6561e-14	11.55	11.55	5.9473e-15	0.240	0.015	0.228	0.023

Table 6. Obtained values of $P_{SR}^{\%}$ and corresponding computation time for planar NTMAs for different possible combinations of (a, b) of $e(\theta, \phi)$ (Intel Core i5-4690 CPU @ 3.50 GHz, RAM: 4 GB).

Sl No.	(a, b)	P_{SR}%						Computation time (sec)			
		ND-NTMA			*D-NTMA*			ND-NTMA		D-NTMA	
		NI	SE	Error	NI	SE	Error	NI	SE	NI	SE Eq. (26.1)-(26.9)
1	(0,0)	26.19	26.19	6.507e-16	26.82	26.82	4.012e-15	3.51	0.008	5.2	0.031
2	(0.5,0)	26.28	26.28	5.5511e-17	26.99	26.99	5.5511e-17	3.36	0.017	5.29	0.033
3	(1,0)	23.94	23.94	6.3838e-16	25.26	25.26	2.2204e-16	3.33	0.01	5.26	0.033
4	(0,0.5)	31.35	31.35	1.993e-15	30.71	30.71	1.5277e-14	3.42	0.018	5.27	0.037
5	(0.5,0.5)	38.64	38.64	2.898e-15	36.83	36.83	2.4253e-14	2.6	20	5.27	27.758
6	(1,0.5)	33.35	33.35	2.415e-15	32.72	32.72	1.9945e-15	2.63	0.018	5.25	0.039
7	(0,1)	32.22	32.22	3.0117e-15	31.18	31.18	2.3028e-15	2.65	0.008	5.26	0.034
8	(0.5,1)	58.32	58.32	1.1102e-16	53.98	53.98	1.1102e-16	2.57	0.020	5.28	0.043
9	(1,1)	52.01	52.01	2.2204e-15	48.56	48.56	1.4433e-15	2.96	0.008	5.25	0.116

and its corresponding simplified expressions (26.1)–(26.9) in (24(b)). The obtained values along with their respective computation time are listed in Table 6. Looking into Table 6, it is observed that almost accurate results with error about less than 10^{-14} are obtained with significantly less computation time directly by using the simplified expressions. However, similar to the linear array, for the case with $a = 0.5$, $b = 0.5$, the computation time becomes relatively higher due to the presence of hypergeometric function.

3.3. Volumetric Array

Let us consider a concentric type volumetric array with array parameters such as element locations, number of rings, number of elements per ring, excitation amplitudes, and normalized on time durations of the elements same as in [42]. For ND-NTMA, the calculation using NI is done in the same way as that for the linear and planar arrays. For D-NTMA, solving the integrals of I_1 in (16(a)), I_3 in (21), and the integral of (10(a)) with summation over N, P_{SR} is calculated using (23(b)) and (24(a)). Without integration, the derived expression in (24(b)) with simplified expressions in (24.1)–(24.9) is utilized considering the order of the Maclaurin series 's' in the range of $0 \leq s \leq 9$, and the obtained results are listed in Table 7. Here also, for the cases with $(a, b) = (0.5, 0)$, $(0.5, 0.5)$, and $(0.5, 1)$,

Table 7. Obtained values of $P_{SR}^{\%}$ and corresponding computation time for volumetric NTMAs for different possible combinations of (a, b) of $e(\theta, \phi)$ (Intel Core i5-4690 CPU @ 3.50 GHz, RAM: 4 GB).

Sl No.	(a, b)	$P_{SR}\%$						Computation time (sec)			
		ND-NTMA			D-NTMA			ND-NTMA		D-NTMA	
		NI	SE	Error	NI	SE	Error	NI	SE	NI	SE Eq. (24.1)-(24.9)
1	(0,0)	40.14	40.14	1.521e-14	40.02	40.02	2.8893e-11	19.21	0.004	21.23	0.38
2	(0.5,0)	39.27	39.27	1.582e-11	39.14	39.14	2.3782e-14	19.38	0.02	21.3	84
3	(1,0)	38.55	38.55	2.493e-14	38.33	38.33	1.3545e-14	18.97	0.01	21.26	0.55
4	(0,0.5)	42.78	42.78	1.386e-11	42.95	42.95	2.7989e-11	18.97	0.013	22.45	0.38
5	(0.5,0.5)	42.23	42.23	2.249e-15	42.61	42.61	1.2398e-14	19.14	21.2	21.36	92
6	(1,0.5)	41.49	41.49	2.591e-15	41.86	41.86	2.8311e-15	19.48	0.023	21.24	0.58
7	(0,1)	43.74	43.74	2.7167e-14	43.84	43.84	2.7167e-10	19.7	0.04	22.16	0.40
8	(0.5,1)	43.6	43.6	2.597e-11	44.05	44.05	1.5923e-14	19.5	0.027	21.91	90
9	(1,1)	42.94	42.94	1.738e-15	43.44	43.44	2.8311e-15	19.35	0.01	21.30	0.60

for which hypergeometric function is present in their respective simplified expressions in (24.2), (24.5), and (24.8), long computation time is required for calculating $P_{SR}^{\%}$. However, for the other cases, the computation time is comparatively less. It is to be mentioned that the utilization of (24.1)–(24.9) for the calculation of $P_{SR}^{\%}$ yields error less than 10^{-10} even though the first 10 polynomials of the Maclaurin series are considered.

To investigate the computation efficiency of the derived expressions for the larger number of antenna elements, a fixed element pattern with $a = 1$, $b = 1$ is taken, and the number of array elements is increased. The results obtained with linear, planar, and volumetric geometries of the arrays are displayed in Table 8. It clearly shows that, with the increased array elements, for any arbitrary array geometry, though computation time for both the methods are increasing, the derived expressions take considerably less time than the numerical integration. It can be further observed that, for the larger arrays, the derived expressions provide more accurate results with reduced errors in their calculated values. The demonstrated results exhibit the efficacy of the derived expressions in accurately computing the power with relatively less time, specifically for the large arrays wherein excessively large time is required for NI.

Table 8. Accuracy in $P_{SR}^{\%}$ calculation and computation time requirement with the increasing number of elements (Intel Core i5-4690 CPU @ 3.50 GHz, RAM: 4 GB).

Geometry	No. of Elements	$P_{SR}\%$						Computation Time (sec)			
		ND-NTMA			D-NTMA			ND-NTMA		D-NTMA	
		NI	SE	Error	NI	SE	Error	NI	SE	NI	SE
Linear	25	5.77	5.77	2.6561e-15	11.55	11.55	5.9473e-15	0.240	0.015	0.228	0.023
	100	3.10	3.10	1.288e-14	6.07	6.07	1.2145e-14	3.491	0.1	0.378	0.147
	225	1.27	1.27	2.549e-13	2.12	2.12	4.2194e-14	16.8	0.555	15.5	0.689
	400	0.069	0.069	4.128e-13	1.34	1.34	7.9271e-13	54.23	1.667	48.88	2.16
Planar	25	52.01	52.01	2.2204e-16	48.56	48.56	1.4433e-15	2.957	0.008	5.25	0.116
	100	9.09	9.09	6.383e-16	6.53	6.53	8.4655e-16	40.66	0.10	42.48	0.1567
	225	3.35	3.35	4.163e-15	2.52	2.52	1.3878e-15	207.75	0.57	212.54	0.695
	400	1.62	1.62	5.447e-16	0.83	0.83	1.5391e-15	627.01	1.8	658.9	2.1947
Volumetric	25	29.19	29.19	2.583e-15	29.75	29.75	1.7258e-16	5.8	0.3	6.7	0.2
	100	33.8	33.8	3.6421e-15	33.75	33.75	6.4791e-15	77	2.2	85	2.1
	225	49.3	49.3	1.1461e-16	49.94	49.94	2.2415e-16	490	7	529	9
	400	53.62	53.62	1.7492e-16	54.5	54.5	4.1784e-16	1548	27	1582	29

4. CONCLUSION

Considering the pulse shifted switching scheme, the closed form expression of sideband power of NTMA is derived by dealing with the ϕ-plane omnidirectional arbitrary element pattern of form $\sin^a\theta\,|\cos\theta|^b$, $a > -1$, $b > -1/2$. Corresponding to the three array geometries — linear, planar, and volumetric, relevant numerical results exemplify the computational proficiency of the derived simplified expressions without hypergeometric function to accurately compute the power. However, for some cases, existence of the hypergeometric function leads to increasing the computation time.

ACKNOWLEDGMENT

This work is financially supported by the Ministry of Electronics and Information Technology (MeitY), Govt. of India under Visvesvaraya Young Faculty Fellowship of Visvesvaraya Ph.D. scheme (Grant No. PhD-MLA-4(29)/2015-16) and the work is under DST-SERB project Ref. file number EEQ/2016/00836, dated January 17, 2017.

REFERENCES

1. He, C., Q. Chen, A. Cao, J. Chen, and R. Jin, "Application of the time modulated array in satellite communications," *IEEE Wireless Commun.*, Vol. 26, No. 2, 24–30, Apr. 2019.
2. Nusenu, S. Y., W. Wang, and A. Basit, "Time-modulated FD-MIMO array for integrated radar and communication systems," *IEEE Antennas Wireless Propag. Lett.*, Vol. 17, No. 6, 1015–1019, Jun. 2018.
3. Rocca, P., F. Yang, L. Poli, and S. Yang, "Time-modulated array antennas — theory, techniques, and applications," *J. Electromagn. Waves Appl.*, Vol. 33, No. 12, 1503–1531, Sep. 2019.
4. Kummer, W., A. Villeneuve, T. Fong, and F. Terrio, "Ultra-low sidelobes from time-modulated arrays," *IEEE Trans. Antennas Propag.*, Vol. 11, No. 6, 633–639, Nov. 1963.
5. Ni, G., C. He, J. Chen, Y. Liu, and R. Jin, "Low sideband radiation beam scanning at carrier frequency for time-modulated array by non-uniform period modulation," *IEEE Trans. Antennas Propag.*, Vol. 68, No. 5, 3695–3704, May 2020.
6. Mandal, S. K., G. Mahanti, and R. Ghatak, "Synthesis of simultaneous multiple-harmonic-patterns in time-modulated linear antenna arrays," *Progress In Electromagnetics Research M*, Vol. 34, 135–142, 2014.
7. Chakraborty, A., G. Ram, and D. Mandal, "Multibeam steered pattern synthesis in time-modulated antenna array with controlled harmonic radiation," *Int. J. RF Microw. Comput. Eng.*, Vol. 31, No. 5, e22597, 2021.
8. Chen, J., et al., "Direction finding based on time-modulated array with multiharmonic analysis," *IEEE Trans. Antennas Propag.*, Vol. 68, No. 7, 5753–5758, Feb. 2020.
9. Xie, X. and Z. Xu, "Direction finding of BPSK signals using time-modulated array," *IEEE Microw. Compon. Lett.*, Vol. 28, No. 7, 618–620, Jul. 2018.
10. Youn, Y., J. Kim, S. Oh, and S. H. Yi, "Time-modulated array system controlled with bipolar squared periodic sequence for direction of arrival estimation," *IEEE Wireless Commun. Lett.*, Vol. 10, No. 9, 1895–1898, Sep. 2021.
11. Mukherjee, A., S. K. Mandal, and R. Ghatak, "Efficient computational method for fast extraction of faulty elements from multipattern time-modulated arrays," *IEEE Trans. Antennas Propag.*, Vol. 69, No. 4, 1982–1991, Apr. 2021.
12. Rocca, P., Q. Zhu, E. T. Bekele, S. Yang, and A. Massa, "4-D arrays as enabling technology for cognitive radio systems," *IEEE Trans. Antennas Propag.*, Vol. 62, No. 3, 1102–1116, Mar. 2014.
13. Ni, D., S. Yang, Y. Chen, and J. Guo, "A study on the application of subarrayed time-modulated arrays to MIMO radar," *IEEE Antennas Wireless Propag. Lett.*, Vol. 16, 1171–1174, Nov. 2016.

14. Chang, Y., H. Jiang, L. Wang, and K. Ding, "Tri-band phase switched screen based on time modulation," *Int. J. RF Microw. Comput. Eng.*, Vol. 32, No. 4, e23058, 2022.
15. González-Coma, J. P., R. Maneiro-Catoira, and L. Castedo, "Hybrid precoding with time-modulated arrays for mmwave MIMO systems," *IEEE Access*, Vol. 6, 59422–59437, Oct. 2018.
16. Maneiro-Catoira, R., J. C. Brégains, J. A. García-Naya, and L. Castedo, "On the feasibility of time-modulated arrays for digital linear modulations: a theoretical analysis," *IEEE Trans. Antennas Propag.*, Vol. 62, No. 12, 6114–6122, Dec. 2014.
17. Zhu, Q., S. Yang, R. Yao, and Z. Nie, "Directional modulation based on 4-D antenna arrays," *IEEE Trans. Antennas Propag.*, Vol. 62, No. 2, 621–628, Feb. 2014.
18. He, C., H. Yu, X. Liang, J. Geng, and R. Jin, "Sideband radiation level suppression in time-modulated array by nonuniform period modulation," *IEEE Antennas Wireless Propag. Lett.*, Vol. 14, 606–609, 2015.
19. Guo, J., S. Yang, Y. Chen, P. Rocca, J. Hu, and A. Massa, "Efficient sideband suppression in 4-D antenna arrays through multiple time modulation frequencies," *IEEE Trans. Antennas Propag.*, Vol. 65, No. 12, 7063–7072, Dec. 2017.
20. Gassab, O., A. Azrar, A. Dahimene, and S. Bouguerra, "Efficient mathematical method to suppress sidelobes and sidebands in time-modulated linear arrays," *IEEE Antennas Wireless Propag. Lett.*, Vol. 18, No. 5, 836–840, May 2019.
21. Yang, J., W. Li, and X. Shi, "Phase modulation technique for four-dimensional arrays," *IEEE Antennas Wireless Propag. Lett.*, Vol. 13, 1393–1396, Jul. 2014.
22. Ni, G., C. He, and R. Jin, "An improved modulation module in time-modulated array," *IEEE Antennas Wireless Propag. Lett.*, 1–1, 2021.
23. Poli, L., P. Rocca, L. Manica, and A. Massa, "Pattern synthesis in time-modulated linear arrays through pulse shifting," *IET Microw. Antennas Propag.*, Vol. 4, No. 9, 1157–1164, Sep. 2010.
24. Aksoy, E. and E. Afacan, "Sideband level suppression improvement via splitting pulses in time modulated arrays under static fundamental radiation," *PIERS Proceedings*, 364–367, Suzhou, China, Sep. 2011.
25. Yang, S., Y. B. Gan, A. Qing, and P. K. Tan, "Design of a uniform amplitude time modulated linear array with optimized time sequences," *IEEE Trans. Antennas Propag.*, Vol. 53, No. 7, 2337–2339, 2005.
26. Zhu, Q., S. Yang, L. Zheng, and Z. Nie, "Design of a low sidelobe time modulated linear array with uniform amplitude and sub-sectional optimized time steps," *IEEE Trans. Antennas Propag.*, Vol. 60, No. 9, 4436–4439, Jul. 2012.
27. Poli, L., P. Rocca, and A. Massa, "Sideband radiation reduction exploiting pattern multiplication in directive time-modulated linear arrays," *IET Microw. Antennas Propag.*, Vol. 6, No. 2, 214–222, Jan. 2012.
28. Mandal, S., G. Mahanti, and R. Ghatak, "Design of a time-modulator to synthesize different patterns in time-modulated antenna arrays," *Journal of Electromagnetic Waves and Applications*, Vol. 28, No. 9, 1118–1130, Oct. 2014.
29. Zhang, S. R., Y. X. Zhang, and C. Y. Cui, "Efficient multiobjective optimization of time-modulated array using a hybrid particle swarm algorithm with convex programming," *IEEE Antennas Wireless Propag. Lett.*, Vol. 19, No. 11, 1842–1846, Nov. 2020.
30. Yang, S., Y. B. Gan, and A. Qing, "Sideband suppression in time-modulated linear arrays by the differential evolution algorithm," *IEEE Antennas Wireless Propag. Lett.*, Vol. 1, 173–175, 2002.
31. Poli, L., P. Rocca, L. Manica, and A. Massa, "Handling sideband radiations in time-modulated arrays through particle swarm optimization," *IEEE Trans. Antennas Propag.*, Vol. 58, No. 4, 1408–1411, Apr. 2010.
32. Fondevila, Bregains, Ares, and Moreno, "Optimizing uniformly excited linear arrays through time modulation," *IEEE Antennas Wireless Propag. Lett.*, Vol. 3, 298–301, 2004.
33. Tong, Y. and A. Tennant, "Reduced sideband levels in time-modulated arrays using half-power sub-arraying techniques," *IEEE Trans. Antennas Propag.*, Vol. 59, No. 1, 301–303, Nov. 2010.

34. Tong, Y. and A. Tennant, "Sideband level suppression in time-modulated linear arrays using modified switching sequences and fixed bandwidth elements," *Electron. Lett.*, Vol. 48, No. 1, 10–11, Jan. 2012.
35. Mukherjee, A., S. K. Mandal, and R. Ghatak, "Differential evolution to synthesize low sidelobe thinned isophoric time-modulated planar array with increased directivity," *Int. J. RF Microw. Comput. Eng.*, Vol. 29, No. 11, e21938, 2019.
36. Bregains, J. C., J. Fondevila-Gomez, G. Franceschetti, and F. Ares, "Signal radiation and power losses of time-modulated arrays," *IEEE Trans. Antennas Propag.*, Vol. 56, No. 6, 1799–1804, Jun. 2008.
37. Aksoy, E. and E. Afacan, "Calculation of sideband power radiation in time-modulated arrays with asymmetrically positioned pulses," *IEEE Antennas Wireless Propag. Lett.*, Vol. 11, 133–136, Jan. 2012.
38. Poli, L., P. Rocca, L. Manica, and A. Massa, "Time modulated planar arrays-Analysis and optimisation of the sideband radiations," *IET Microw., Antennas Propag.*, Vol. 4, No. 9, 1165–1171, Sep. 2010.
39. Aksoy, E., "Calculation of sideband radiations in time-modulated volumetric arrays and generalization of the power equation," *IEEE Trans. Antennas Propag.*, Vol. 62, No. 9, 4856–4860, Sep. 2014.
40. Bekele, E. T., L. Poli, P. Rocca, M. D. Urso, and A. Massa, "Pulse-shaping strategy for time modulated arrays — Analysis and design," *IEEE Trans. Antennas Propag.*, Vol. 61, No. 7, 3525–3537, Jul. 2013.
41. Zeng, Q., et al., "Calculation of the total radiated power for 4-D antenna arrays with arbitrary time modulated waveform," *IEEE Trans. Antennas Propag.*, Vol. 69, No. 12, 9015–9020, Dec. 2021.
42. Zeng, Q., P. Yang, H. Lin, F. Yang, and S. Yang, "Generalized closed-form sidebands' radiation expressions for 4-D antenna arrays," *IEEE Trans. Antennas Propag.*, Vol. 69, No. 2, 1193–1197, Feb. 2021.
43. Kanbaz, I., U. Yesilyurt, and E. Aksoy, "A study on harmonic power calculation for nonuniform period linear time modulated arrays," *IEEE Antennas Wireless Propag. Lett.*, Vol. 17, No. 12, 2369–2373, Dec. 2018.
44. Mandal, S. and S. K. Mandal, "Harmonic power losses in time-modulated arrays with non-uniform period modulation," *AEU — Int. J. Electron. Commun.*, Vol. 108, 45–52, Aug. 2019.
45. Kanbaz, I., U. Yesilyurt, S. Kuzu, and E. Aksoy, "Total harmonic power of arbitrarily switched nonuniform period time-modulated arrays," *IEEE Antennas Wireless Propag. Lett.*, Vol. 19, No. 1, 193–197, Jan. 2020.
46. Yesilyurt, U., I. Kanbaz, and E. Aksoy, "Effect of ground plane on power losses and efficiency for uniform period time modulated arrays," *IEEE Sensors J.*, Vol. 22, No. 4, 3637–3647, Feb. 2022.
47. Yesilyurt, U., I. Kanbaz, and E. Aksoy, "Power losses and efficiency analysis of non-uniform time modulated arrays over a ground plane," *AEU-Int. J. Electron. Commun.*, Vol. 146, No. 154106, Mar. 2022.
48. Manica, L., P. Rocca, L. Poli, and A. Massa, "Almost time-independent performance in time-modulated linear arrays," *IEEE Antennas Wireless Propag. Lett.*, Vol. 8, 843–846, 2009.
49. Blinder, S. M., "Chapter 13 — Partial differential equations and special functions," in *Guide to Essential Math (2nd Edition)*, S. M. Blinder, Ed., 227–251, Elsevier, Oxford, 2013.
50. Pearson, J. W., *Computation of Hypergeometric Functions*, University of Oxford, 2009.
51. Watson, G. N., *A Treatise on the Theory of Bessel Functions*, Cambridge Univ. Press, Cambridge, UK, 1995.